EURASIAN JOURNAL OF MATHEMATICAL AND COMPUTER APPLICATIONS
ISSN 2306–6172
Volume 13, Issue 1 (2025) 64– 78

CFD-DEM SIMULATION OF THE HYDRODYNAMICS OF A DISPERSED GAS-SOLID FLOW WITH IRREGULAR BIOMASS PARTICLES

Ershov M. I. [1] , **Abaimov N. A.** , **Nikitin A. D.** , **Tuponogov V. G.** , **Ryzhkov A. F.**

Abstract A CFD-DEM model of irregularly shaped particle movement in a dispersed gas-solid flow was tested and validated against experimental data for a spouted bed of sawdust with a particle size fraction of 1-1.2 mm (Geldart D) in a pseudo-2D prismatic setup with the features of the flow section of a pilot-scale sawdust gasification unit. The movement of three particle sets, including spherocylinders and/or plates, was modeled using the two-way coupling of CFD-DEM methods. The Holzer/Sommerfeld drag model for non-spherical particles, with Di Felice porosity correction were implemented. The simulation results showed good agreement with the experimental data at moderate air velocities (1.3 and 1.9 m/s) and deviation from the experiment at high air velocities (3.1, 4.6, and 5.4 m/s). Replacing plates with spherocylinders improved the agreement of some parameters with the experiment; however, at high air velocities, the symmetric bottom layer was less stable.

Key words: biomass, non-spherical particle, Computational Fluid Dynamics, Discrete Element Modeling.

AMS Mathematics Subject Classification: 76M25; 76F25; 74E20.

DOI: 10.32523/2306-6172-2025-13-1-64-78

1 Introduction

In the context of the energy transition, biomass, as a carbon-neutral fuel, replaces traditional fossil fuels. One of the most efficient ways to utilize biomass including wood sawdust in energy and chemical technology is the conversion of combustible components of the original fuel into a gaseous or liquid state. To produce syngas from wood sawdust in the gasifier reaction chamber, it is necessary to create the multiphase hydrodynamic flow regimes that ensure uniform agglomeration-free distribution of solid particles throughout the chamber volume [1, 2] and sufficient residence time for the entire polydisperse composition of the particles.

Special attention must be given to the shape of particles when developing reactor processes. The commonly used coarse materials, such as crushed coal or alumina ceramics [3], which belong to Group D according to Geldart's classification [4], typically have relatively spherical particle shapes and comparatively high density. When using fuel biomass, including wood sawdust, it is necessary to work with very light, irregularly shaped particles (such as plate-like or needle-like shapes), for which the drag coefficient

[1]Corresponding Author.

significantly depends not only on the particle shape but also on their orientation relative to the flow direction. Such particles have very low sphericity coefficient and are extremely polydisperse [5, 6]. Another characteristic of biomass particles, particularly wood sawdust, is their increased roughness [7].

Existing numerical models for studying multiphase flows can be divided into two main groups: the Euler-Euler method (or two-fluid model, TFM) and the Euler-Lagrange method [8, 9]. These models are widely used for simulating dispersed gas-solid flows in various fluidized bed and pneumatic transport systems. In both approaches, the gas phase is considered a continuous medium, while the solid particles are modeled differently. The Euler-Euler method assumes that the solid phase can be treated as an interpenetrating continuous medium with representative properties similar to those of a fluid. For adequate modeling of particle movement and collisions, reasonable assumptions must be made regarding the drag between the gas and solid phases and the rheology of the solid phase. This requires additional closure equations for particle interactions, for which the Kinetic Theory of Granular Flows was developed [10].

In the Euler-Lagrange method, the solid phase is tracked in Lagrangian space, and the movement of each individual element is calculated based on Newton's second law. Compared to the Euler-Lagrange method, the Euler-Euler method has a simpler computational scheme and requires fewer computational resources [11], which is advantageous for practical applications in industrial systems. However, as the number of particle sizes and/or materials considered increases, the computational costs of the Euler-Euler method rise due to the increased number of equations to be solved [9]. The Euler-Lagrange method, on the other hand, allows for detailed information about particles (movement trajectories, orientations, collisions, component composition, user-defined scalars) [12, 13], and its results usually align better with experimental data due to improved particle rheology descriptions and reduced numerical errors, such as numerical diffusion [14, 8]. Today, with the advancement of software capabilities and computational power, and the transition to particle motion calculations on GPUs, the Euler-Lagrange method is gaining popularity. This method is implemented in the Ansys Fluent Rocky DEM coupling for calculating fluidized bed and pneumatic transport systems [15].

An elongated non-spherical particle in a gas flow, without chemical transformations and external forces except for gravity, is generally subjected to drag force, lift force, and hydrodynamic torque. Universal laws have been derived for the drag force on a single irregularly shaped particle, which can adequately describe even plate-like particles [16, 17]. However, there are still no sufficiently accurate drag laws that account for the volume fraction and polydisperse granulometric composition of non-spherical particles. For instance, the law [18] is applicable only to ellipsoids of identical shape and size. For the sake of simplification, some researchers [19, 20] prefer to apply the Di Felice porosity correction for spherical particles [21] combined with the drag law for a single non-spherical particle by Holzer/Sommerfeld [17]. Separate laws have also been derived for the lift force and hydrodynamic torque [22, 23]. However, these are mainly suitable only for ellipsoids and spherocylinders, fail to account for the effects of volume concentration and polydisperse granulometric composition, and are inconvenient to use as they contain many empirical coefficients, which are calibrated for specific particle

types based on individual CFD calculations.

The impact of particle roughness on its aerodynamic properties under various flow conditions is not fully covered in the scientific community. The effect of the surface roughness of plate-like sawdust particles compared to equivalent smooth plates on the drag coefficient has not been found in the literature. However, it is well-established that in pneumatic transport conditions, smooth bodies have a higher terminal velocity than rough bodies because the drag coefficient is higher for the latter [24]. Also, increasing the surface roughness of a particle up to 100 μm reduces its aerodynamic diameter [25]. Additionally, for a fixed bed of large particles in the form of spheres, cylinders, and Raschig rings with an equivalent diameter of 20 mm under confined flow conditions, a correction factor for the Ergun equation has been derived through experimental and numerical methods. This correction factor adjusts the pressure drop considering the particle roughness and air flow velocity [26].

This paper presents the results of the calculation of fluidization for three different sets of polyhedral particles, simulating sawdust with a sieve size of 1-1.2 mm, in a pseudo-2D prismatic setup with a conical bottom part having an angle of 38B° and a rectangular upper part, for five air inlet velocities ranging from 1.3 to 5.4 m/s. The flow section of the investigated unit is similar to that used in the pilot-scale sawdust gasifier at the Laboratory of New Energy Technologies of the Ural Federal University. The CFD-DEM calculations employ the Holzer/Sommerfeld drag law with Di Felice porosity correction. Lift force and torque from interaction with the flow are neglected. The results are compared with experimental data.

2 Experimental part

The pseudo-2D cold model of the pilot-scale gasifier consists of an air supply section (at the bottom), a conical section, a rectangular section, and an outlet section with a dispersed gas-solid flow directed to a filter. The cone has an opening angle of 38B°, the largest cross-section is 500x20 mm, and the inlet cross-section is 50x20 mm. The experimental setup is equipped with a measurement system that allows video recording of the dispersed flow structure and computer recording of digital pressure fluctuation data for subsequent statistical processing in Matlab. Pressure fluctuation measurements were taken at a height of 30 mm above the grid (entry to the conical section)

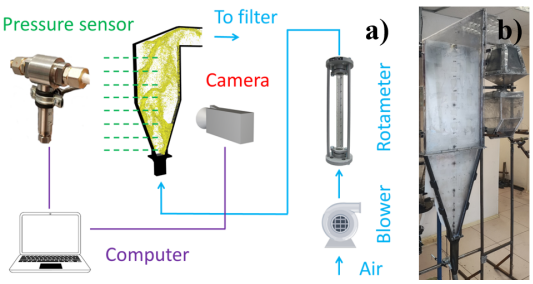

Figure 1: Experimental setup: a - schematic diagram; b- experimental unit photograph

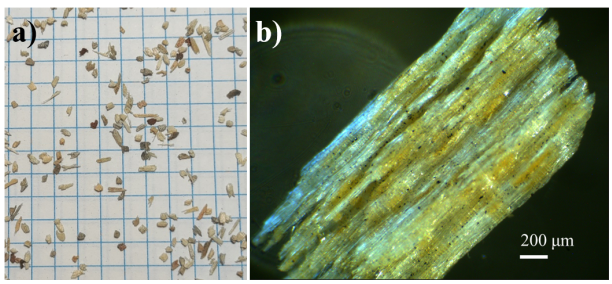

Figure 2: Particle images: a - group of particles; b -individual particle

using a Keller PD-33X sensor with a sampling rate of 32 Hz. A schematic diagram of the laboratory setup and a photograph of the installation are shown in Fig. 1. The material of the setup walls is polystyrene. The most important dimensions for modeling are provided later in the CFD-DEM modeling methodology section.

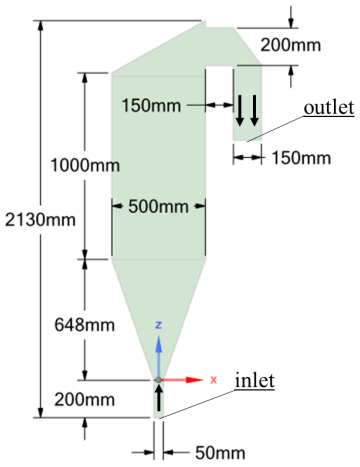

Figure 3: Geometric model of the computational domain with applied boundary conditions

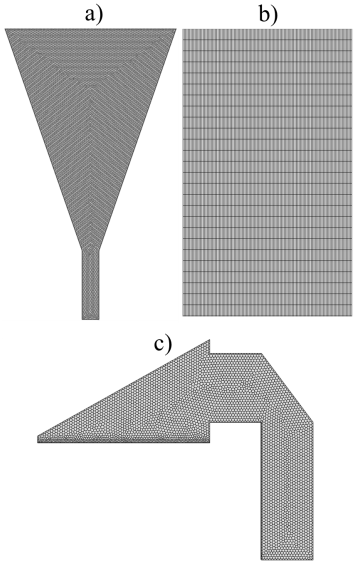

Figure 4: Components of the computational domain mesh: a - lower conical part with inlet; b - middle straight part; c - outlet part

Experiments on pressure fluctuation were conducted for a fraction of sawdust separated using sieves with mesh sizes of 1.0 and 1.2 mm in the laboratory granulometric analysis complex. Particles up to 6 mm in length could pass through the upper sieve. These particles fall into Group D according to Geldart's classification. The experiment was carried out at room temperature. The initial bed height was 50 mm. The inlet velocity was set to 1.3, 1.9, 3.1, 4.6, and 5.4 m/s. Each velocity test lasted for 40 seconds. The bulk density of the sawdust particles was 147.6 $\mathrm{kg/m^3}$ when poured into a measuring cylinder with shaking and 169.1 $\mathrm{kg/m^3}$ when the material was compressed in the cylinder with a rod. Assuming a particle volume concentration of 0.5, the apparent density of the particles can vary between $295.2 - 338.2\,\mathrm{kg/m^3}$, due to the high fragmentation of the particle body, creating increased roughness. An image of a particle group and an individual particle microscopic image are shown in Fig. 2.

For the obtained pressure signals, the root mean square deviation is analyzed: $s = \sqrt{\frac{1}{N-1}\sum_{i=1}^{N}(x_i - x_m)^2}$, where N is the number of the last sampling point in the analyzed dataset, i is the number of the current sampling point ($i = 1, \ldots, N$), x_i is the value of the current sampling point, x_m is the mean value of the dataset: $x_m = \frac{1}{N}\sum_{i=1}^{N} x_i$; and the amplitude-frequency spectrum using the discrete Fourier transform, where each discrete frequency f_n is calculated using the formula: $f_n = \frac{n}{N\Delta t}$, where Δt is the time interval between two consecutive points in the data series, n is the index that denotes the number of the discrete frequency ($n = 0, \ldots, N-1$), the spectral component X_n for each frequency is calculated using the formula: $X_n = \sum_{q=0}^{N-1} x_q \exp\left(-j\frac{2\pi nq}{N}\right)$, where q is the number of the current sampling point ($q = 0, \ldots, N-1$), x_q is the value of the current sampling point, j is the imaginary unit, π is the number of Pi.

3 Numerical modeling methods

The interaction of the particle groups with the gas flow is modeled using the combination of CFD and DEM methods (CFD-DEM modeling), where the CFD method is responsible for modeling the gas flow, and the DEM method is responsible for tracking the particles and the mechanics of particle-flow and particle-particle interactions. The model is based on a two-way coupling of the CFD solver for describing continuous flow in Ansys Fluent®2021 R1 and the DEM solver for modeling the behavior of irregularly shaped biomass particles in Rocky DEM 2021 R1.

3.1 Geometry and mesh

The geometry, created in Space Claim Direct Modeler with the designated boundary conditions for the inlet and outlet, is shown in Fig. 3. The thickness of the computational domain is 20 mm.

The mesh for the computational domain consists of three parts (Fig. 4). The lower conical part (Fig. 4(a)) with air inlet includes polyhedral cells with an equivalent sphere diameter of 2-5 mm, totaling 97,487 cells. The middle straight section (Fig. 4(b)) consists of structured elongated rectangular parallelepipeds with dimensions of 32.67x4x4 mm, totaling 18,750 cells. The outlet section (Fig. 4(c)) includes polyhedral cells with an equivalent sphere diameter of 3-8 mm, totaling 22,584 cells. All mesh parts are connected by non-conformal interfaces. In total, the calculation involves 138,821 cells, with a minimum orthogonal quality of 0.261. In the wall-adjacent region, only one prismatic layer is provided for polyhedral meshes to ensure the cell size exceeds the particle size, thereby avoiding errors in determining the particle volume fraction [9].

3.2 Mathematical model

The turbulent airflow was modeled using the two-parameter k-epsilon model. Thus, the following equations are used to carry out the gas flow numerical simulation using the CFD method: the continuity equation (5), the Navier-Stokes equations (6), the turbulent kinetic energy equation (7), and the dissipation rate equation (8):

$$\begin{aligned}
\frac{\partial}{\partial t}(\alpha\rho) + \nabla(\alpha\rho u) &= 0, \\
\frac{\partial}{\partial t}(\alpha\rho u) + \nabla(\alpha\rho u^2) &= -\alpha\nabla p + \nabla(\alpha T) + \alpha\rho g + S_{pf}, \\
\frac{\partial}{\partial t}(\alpha\rho k) + \nabla(\alpha\rho k u) &= \nabla\left[\alpha\left(\mu + \frac{\mu_t}{\sigma_k}\right)\nabla k\right] + \alpha G_k + \alpha\rho\sigma_k, \\
\frac{\partial}{\partial t}(\alpha\rho\epsilon) + \nabla(\alpha\rho\epsilon u) &= \nabla\left[\alpha\left(\mu + \frac{\mu_t}{\sigma_\epsilon}\right)\nabla\epsilon\right] + \alpha\frac{\epsilon}{k}(C_1 G_k - C_2\rho\epsilon),
\end{aligned}$$

where t -time, α - porosity, ρ - fluid density, u - fluid velocity, p - fluid pressure, T - stress tensor, g - acceleration due to gravity ($9,81\,\mathrm{m/s^2}$), S_{pf} - momentum source from particle-flow interaction, k - turbulent kinetic energy, μ - dynamic viscosity of the gas, μ_t - turbulent viscosity of the gas, $\sigma_k = 1.0$ ΓË $\sigma_\epsilon = 1.33$ - Prandtl constants, G_k -

source of turbulent kinetic energy from averaged velocity gradients, ϵ - dissipation rate, $C_1 = 0.09$ and $C_2 = 1.44$ - empirical constants.

The interaction between particles and the flow is modeled using only the drag force. Lifting force and hydrodynamic torque are not taken into account in the calculations. The drag force F_D equation is $F_D = \frac{\pi}{8} C_D \rho d^2 |u - v|(u - v)\alpha^{1-\beta}$, where C_D - aerodynamic drag coefficient, d - equivalent particle diameter, v - particle velocity, β - Di Felice correction [21] for modelling the influence of porosity around the tracked particle $\beta = 3.7 - 0.65 \exp\left(-\frac{1}{2}(1.5 - \log_{10} \mathrm{Re})^2\right)$, where Re - Reynolds number, calculated by the formula: $\mathrm{Re} = \alpha\rho|u - v|d/\mu$.

The drag coefficient C_D depends on the particle orientation in space and is calculated using the simplified formula by Holzer-Sommerfeld [17]:

$$C_D = \frac{8}{\mathrm{Re}} \frac{1}{\sqrt{\Phi_\perp}} + \frac{16}{\mathrm{Re}} \frac{1}{\Phi} + \frac{3}{\sqrt{\mathrm{Re}}} \Phi^{3/4} + 0.42 \left(10^{0.4(4 - \log_{10} \Phi)}\right)^{0.2} \frac{1}{\Phi_\perp},$$

where Φ is the sphericity coefficient of the particle (the ratio of the surface area of a sphere with equivalent volume to the surface area of the particle), and $\Phi_\perp$ is the crosswise sphericity coefficient of the particle (the ratio of the cross-sectional area of a sphere with equivalent volume to the cross-sectional area of the particle projected onto a plane perpendicular to the incoming flow).

In DEM modeling, particles are tracked and moved using the Lagrangian method. The contact interaction is described by the Hysteretic Linear Spring law for the normal force component and the Linear Spring Coulomb Limit for the tangential force component [9]. The translational and rotational motion of a particle is described by Newton's second law using the following equations:

$$m\frac{dv}{dt} = F_D + F_C + mg, \qquad I\frac{d\omega}{dt} = M_C,$$

where m is the particle mass, F_C is the contact force, I is the particle moment of inertia, ω is the particle angular velocity, M_C is the contact torque.

The main parameters of CFD and DEM solvers, as well as the mechanical properties of particles, are shown in Tab. 1. The apparent particle density of 300 kg/m^3 is assumed based on the equality of the mass of the bed of virtual particles with a height of 50 mm to the mass of a similar bed of sawdust, which corresponds to the observations [27]. The energy recovery coefficient is assumed to be 0.5, as in the work [19]. Young's modulus for sawdust is assumed to be equal to 360000 Pa, as for dry birch sawdust [28]. The Poisson's ratio is assumed to be 0.35, as in the study [29]. The friction coefficients in particle-particle and particle-wall pairs are assumed to be 1.0 and 0.9, which is due to the high roughness of the sawdust particles and is confirmed by calibration tests.

Six different particle types of two shapes are used in the simulation (Fig. 5): three types of plates and three types of spherical cylinders. Each shape has the same cross-section and three different lengths. For plates, the width is 1.10 mm, and the thickness is 0.33 mm. For spherical cylinders, the diameter is assumed to be 1.10 mm. Three particle lengths of 5.50, 3.30 and 1.65 mm are used. The width and diameter were assumed to be the average between the values of the sieves used (1.00 and 1.20 mm) during granulometric tests.

Due to the significant uncertainty in the distribution of particles by shape and size, three sets of particles are investigated: only plates (Plates), plates with 35% of the

Table 1: Parameters used in modeling

Parameter	**Value**
Apparent particle density (kg/m^3)	300
Young's modulus (Pa)	360000
Poisson's ratio	0.35
Restitution coefficient	0.5
Friction coefficient in a particle-particle pair	1.0
Friction coefficient in a particle-wall pair	0.9
Gas density (kg/m^3)	1.204
Gas dynamic viscosity (Pa s)	1.81×10^{-5}
Turbulence intensity at inlet, %	5
Hydraulic inlet diameter, mm	28.57
CFD solver scheme	SIMPLE
Discretization of the transient term	First Order Implicit
Discretization of pressure	Second Order
Discretization of momentum	Second Order Upwind
Discretization of k and ϵ (turbulence)	First Order Upwind
Time step size DEM (s)	1×10^{-6}
Time step size CFD (s)	1×10^{-3}
The maximum number of iterations per CFD time step	50
Convergence criterion of the continuity equation	0.0001

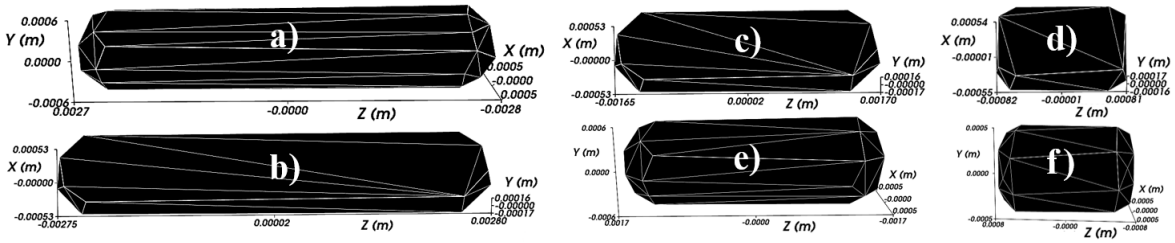

Figure 5: Particles used in simulations: a - spherocylinder, length 5.50 mm; b - plate, length 5.5 mm; c - plate, length 3.3 mm; d - plate, length 1.65 mm; e - spherocylinder, length 3.3 mm; f - spherocylinder, length 1.65 mm

mass replaced by spherocylinders (Plates and spherocylinders (0.35)), and plates with 70% of the mass replaced by spherocylinders (Plates and spherocylinders (0.70)). The total number of particles in the calculations for each of three sets is 36.350, 28.540, and 20.733 units, respectively. The total mass of particles in each set is 10 grams. The mass ratio between particles of different lengths is kept constant. Information on the mass of the particles individually and in the three sets is provided in Tab. 2.

3.3 Initial and boundary conditions

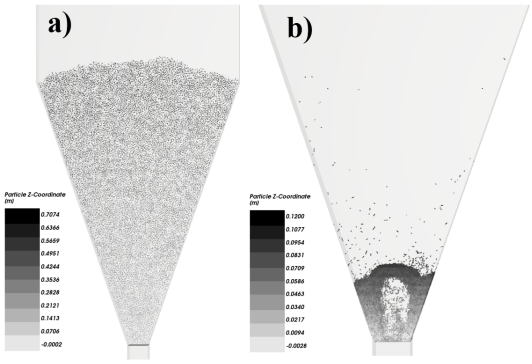

Figure 6: Snapshots of the dispersed gas-solid flow at the beginning of the simulation for a particle set with 35% of the mass replaced by spherocylinders: a B— state of the dispersed gas-solid flow at time $t = 0$ s; b B— state of the dispersed gas-solid flow at time $t = 1$ s. The color scale indicates the height above the beginning of the conical section

For each particle set, a flow time of 21 seconds was simulated. At the 50x20 mm rectangular inlet of the computational domain, a uniform velocity profile was set. From 0 to 1 second, the velocity increased linearly from 0 to 1.3 m/s, then maintained at 1.3 m/s for 4 seconds. At the 5th second, the velocity was set to 1.9 m/s and held for another 4 seconds. Similarly, four-second intervals were set for velocities of 3.1 m/s, 4.6 m/s, and 5.4 m/s. Thus, during the first second, the particle clusters gradually settled at the bottom of the setup, and the system smoothly transitioned into the initial fluidization regime, meaning the dispersed gas-solid system separated into a dense peripheral layer and a less dense central spout. Fig. 6(a) shows the initial particle positions for a particle set with 35% of the mass replaced by spherocylinders, and Fig. 6(b) shows the state of the dispersed gas-solid system after 1 second. When calculating the root mean square deviations and dominant frequencies at each four-second velocity interval, the first 0.5 seconds and the last 0.25 seconds were excluded, meaning intervals of 3.25 seconds were used for stochastic analysis.

4 Results and discussion

Experimental studies indicate the constant presence of a dense symmetrical structure of sawdust at the edges near the bottom of the conical section of the unit at all air inlet velocities, resulting in dominant frequencies of 3.5-6.5 Hz. The simulation results, on

Table 2: Masses of the analyzed particles and particle sets

Particle	Mass, g			
	Separate particle	Plates	Plates and spherocylinders (0.35)	Plates and spherocylinders (0.70)
Plate 5.50 mm	5.293E-4	2.300	1.495	0.690
Plate 3.30 mm	3.081E-4	5.400	3.510	1.620
Plate 1.65 mm	1.589E-4	2.300	1.495	0.690
Spherocylinder 5.50 mm	1.388E-3	0	0.805	1.610
Spherocylinder 3.30 mm	7.919E-4	0	1.890	3.780
Spherocylinder 1.65 mm	4.133E-4	0	0.805	1.610

the other hand, indicate the instability of the gas-solid flow structure at the bottom of the unit at higher air velocities (3.1-5.4 m/s) and the presence of lower dominant frequencies in the spectrum. The following is a comparison of the experimental and CFD-DEM modeling results in terms of root mean square deviation, dominant frequencies for pressure signals at a height of 30 mm from the entrance to the conical section and the maximum vertical coordinate of the particles. It should be noted that in modeling such a complex gas-solid system, deviations from the experiment of up to 15% are considered insignificant, while deviations of 15-30% can be considered satisfactory.

CFD-DEM modeling for plate-like particles showed that at moderate air inlet velocities of 1.3 and 1.9 m/s, gas-solid flow structures similar to those observed in the experiment are formed (Fig. 7). However, the upper boundary of the gas-solid flow appears denser than in the experiment. The similarity of the structures is supported by the quantitative agreement of the dominant frequencies of the pressure signal fluctuations obtained numerically and experimentally at a height of 30 mm (Fig. 8). For example, at a velocity of 1.3 m/s, the dominant frequency obtained from CFD-DEM modeling (4 Hz) corresponds to the lower bound of the dominant frequencies observed in the experiment (3.9-4.9 Hz). At a velocity of 1.9 m/s, the dominant frequency obtained from the simulation is 10% lower than in the experiment (4.1 Hz). The root mean square deviation (Fig. 9) at a velocity of 1.3 m/s is 36.7% higher than the experimental value, while at 1.9 m/s, it is 8.4% lower. The maximum particle peak height at a velocity of 1.3 m/s (Fig. 10) is mostly 3-15% lower than the maximum height observed in the experiment, but in some instances exceeds the experimental value by 24%. For a velocity of 1.9 m/s, the maximum particle peak height in the simulation mostly exceeds the experimental maximum height by 20-44%. With the gradual replacement of 35% and 70% of the mass of plates by spherocylinders, the dominant frequency remains almost unchanged, but the maximum particle peak height decreases. For a particle set with 35% spherocylinders at a velocity of 1.3 m/s, the maximum height is mostly 1-10% lower than the experimental value, and at 1.9 m/s, it is also 1-10% lower, but in some cases, it is 10-23% higher. For a particle set with 70% spherocylinders at a velocity of 1.3 m/s, the maximum height is mostly 20-30% lower than the experimental level, but in some cases, it is only 5-10% lower. At 1.9 m/s, the maximum height is mostly 25-30% lower than the experimental value, but in some cases, it is 5-10% higher.

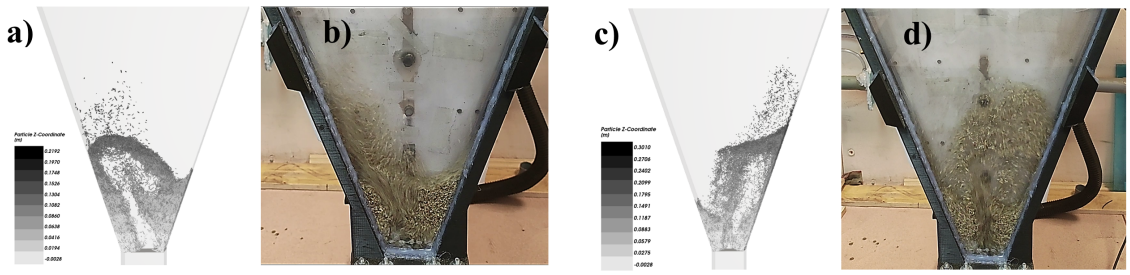

Figure 7: Snapshots of the gas-dispersed flow during the experiment and during CFD-DEM modeling with plates: a B— simulation at an inlet air velocity of 1.3 m/s; b B— experiment at an inlet air velocity of 1.3 m/s; c B— simulation at an inlet air velocity of 1.9 m/s; d B— experiment at an inlet air velocity of 1.9 m/s. The color scale indicates the height above the beginning of the conical section

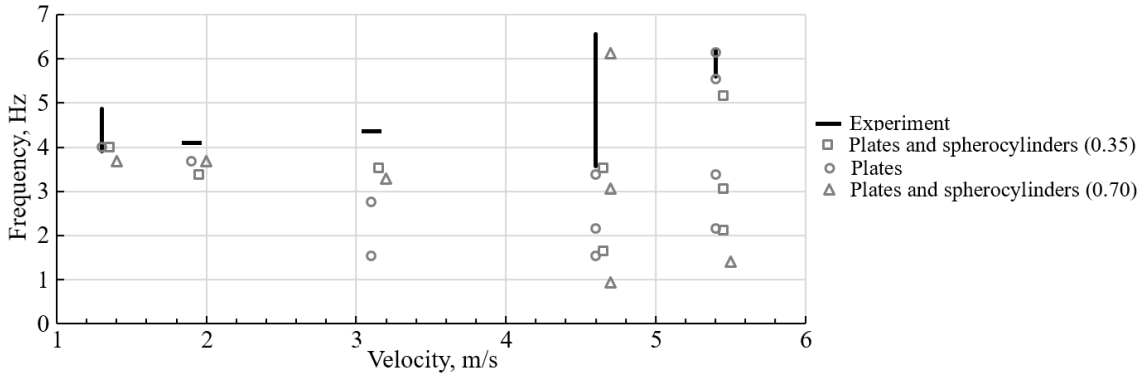

Figure 8: Dominant pressure fluctuation frequencies versus inlet air velocity for the experiment and CFD-DEM modeling with different particle sets. Horizontal black lines indicate a single dominant frequency, and vertical lines indicate a wide spectrum of dominant frequencies in the experiment. Markers represent the dominant frequencies in CFD-DEM modeling. Markers for different particle sets are offset by 0.05 m/s to avoid overlapping

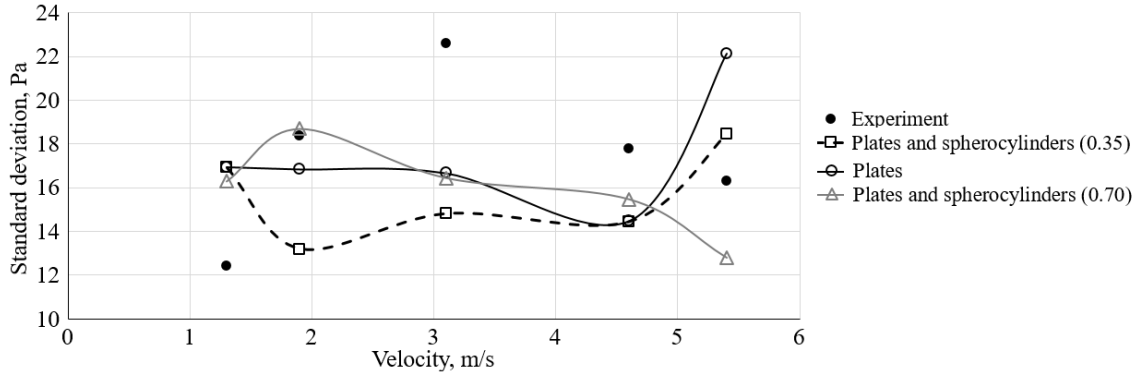

Figure 9: Root mean square pressure fluctuation deviation versus inlet air velocity for the experiment and CFD-DEM modeling with different particle sets. Black dots represent the root mean square deviation in the experiment, and the markers connected by lines represent the root mean square deviation in CFD-DEM modeling

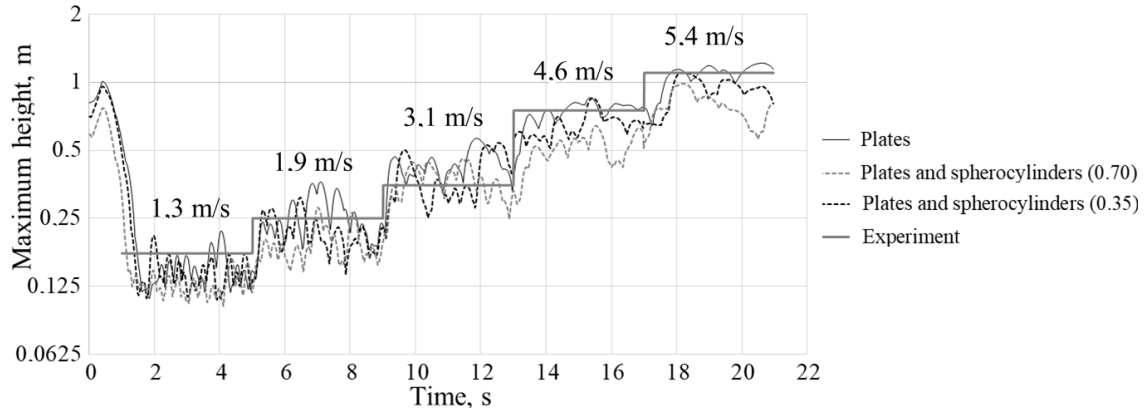

Figure 10: Maximum particle height versus simulation time for CFD-DEM modeling with different particle sets. The gray step line indicates the level of maximum height observed in the experiment

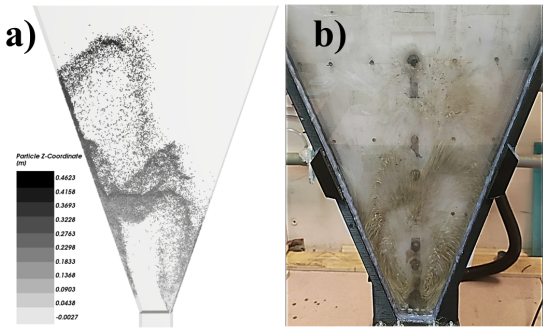

Figure 11: Snapshots of the gas-dispersed flow during the experiment and during CFD-DEM modeling with plates at an inlet air velocity of 3.1 m/s: a - simulation; b - xperiment. The color scale indicates the height above the beginning of the conical section

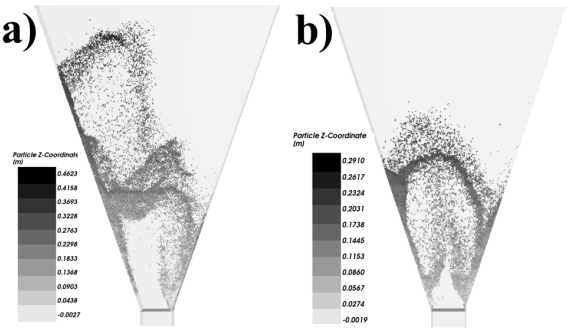

Figure 12: Snapshots of a gas-dispersed flow during CFDB–DEM modeling at an air velocity of 3.1 m/s: a - plates; b - plates with 70% mass replacement by spherocylinders. The color scale indicates the height above the beginning of the conical section

The root mean square deviation at a velocity of 1.3 m/s remains almost unchanged, while at 1.9 m/s, with the addition of 35% spherocylinders, it is 28.2% lower than in the experiment, and with 70% spherocylinders, it approaches the experimental value again (1.7% higher than in the experiment).

CFD-DEM modeling for plate-like particles showed that at the air inlet velocity of 3.1 m/s, the observed gas-solid flow structures significantly differ from those seen in the experiment. The symmetrical peripheral layer at the entrance of the conical section is not able to maintain its structure as it does in the experiment, leading to chaotic clusters of particles being thrown from one wall to another (Fig. 11). With such differences in regimes, the root mean square deviation of the model signal is 26.3% lower than the experimental value (Fig. 9). Instead of a single dominant frequency of 4.367 Hz (Fig. 8), the modeling results show two dominant frequencies (1.54 and 2.77 Hz). The maximum particle peak height is 20-35% higher than in the experiment, with one instance reaching 61% higher (Fig. 10).

With the gradual replacement of 35% and 70% of the mass of plates with spherocylinders, the dominant frequency acquires a single peak (3.53 and 3.29 Hz, respectively). The peak of the maximum particle peak height decreases and becomes 55% and 31% higher than the experimental value, respectively, indicating a closer match to the experimental values. The root mean square deviation also slightly decreases, increasing the discrepancy with the experiment from 26.3% (only plates) to 34.5% and 27.2%, respectively. This convergence to the experiment when plates are replaced with spherocylinders is largely due to the fact that the aerodynamically heavier spherocylinders tend to form a symmetrical periphery at the entrance to the conical section (Fig. 12(b)). However, the bottom layer is not sufficiently massive and stable, resulting in a significant remaining discrepancy with the experiment in terms of root mean square deviation.

At air inlet velocities of 4.6 and 5.4 m/s, none of the simulated particle sets can maintain a symmetrical bottom layer similar to what is observed in the experiment

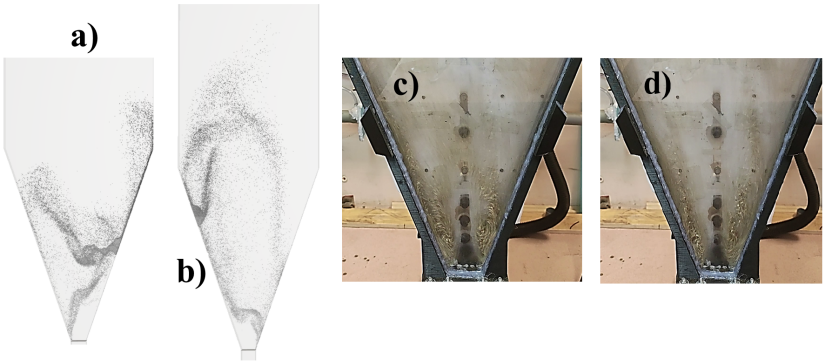

Figure 13: Snapshots of the gas-dispersed flow during the experiment and during CFD-DEM modeling with plates: a - modeling at an inlet air velocity of 4.6 m/s; b - modeling at an inlet air velocity of 5.4 m/s; c - the state of the gas-dispersed flow at the entrance to the conical part at an inlet air velocity of 4.6 m/s; d is the same, at an inlet air velocity of 5.4 m/s. The color scale indicates the height above the beginning of the conical section

(Fig. 13). As with the 3.1 m/s velocity, a chaotic scattering of particle clusters from one wall to another occurs with the plate-like particle set, leading to the appearance of dominant frequencies in the range of 1-3.5 Hz, which are not present in the experiment (Fig. 8). The maximum particle peak height for plates at these velocities corresponds to experimental observations (Fig. 10), with the height exceeding the experimental value by no more than 13% in isolated cases. With the gradual replacement of 35% and 70% of the mass of plates with spherocylinders, the maximum particle peak height significantly decreases. For a particle set with 35% spherocylinders at a velocity of 4.6 m/s, the maximum height is mostly 6.5-20% lower than the experimental value, but in some instances, it is 13% higher. At 5.4 m/s, the maximum height is also 6.5-12.5% lower than the experimental value, but in some instances, it matches the experimental level. For a particle set with 70% spherocylinders at 4.6 m/s, the maximum height is mostly 15-30% lower than the experimental value, and at 5.4 m/s, it is also 10-30% lower. For most particle sets, the root mean square deviation values are significantly closer to the experimental values than at 3.1 m/s (Fig. 9). At 4.6 m/s, the simulation results are 18.5%, 18.8%, and 12.9% lower than the experimental values for the considered particle sets, respectively. At 5.4 m/s, the simulation results are 35.7% and 13.1% higher than the experimental values for the first two particle sets and 21.5% lower for the last particle set. The exception is the plate-like particle set at 5.4 m/s, where the root mean square deviation is 35.7% higher than in the experiment. This higher value of dispersion may be due to episodic pressure spikes caused by particles returning along one of the side walls from a height greater than that observed with other particle sets.

Thus, the modeling of gas-dispersed systems with sawdust using the most popular approach (Holzer/Sommerfeld drag law with the Di Felice porosity correction without lift and hydrodynamic torque laws) yields results closest to the experimental data at moderate air velocities, where the maximum particle height is below five initial bed heights. At more intense regimes, there may be errors in predicting the flow structure and, consequently, the amplitude-frequency characteristics and the maximum particle height.

5 Conclusion

Modeling of the dispersed gas-solid system with Geldart D sawdust particles using the CFD-DEM method showed that the results are closest to the experimental data at moderate air velocities (1.3 and 1.9 m/s). At higher velocities, greater discrepancies with experiments are observed in the flow structure and pressure fluctuation characteristics. Replacing plates with spherocylinders improves the agreement of some parameters with the experiment, but maintaining a symmetrical bottom layer remains problematic at high velocities. Thus, the CFD-DEM approach has proven to be quite successful as the first step to modelling such complex system and can be adopted as a basis when more accurate prediction of dispersed gas-solid flow characteristics under various operating conditions is needed.

To clarify the orientation of particles relative to the flow at various flow velocities and particle volume concentrations, it is necessary to set up a task involving the movement of a group of unbounded particles in an upward flow using Overset Mesh or Dynamic Mesh methods. This should be done with different turbulence modeling options (Reynolds-averaged Navier-Stokes equations (k-w SST, Reynolds Stress Model) and Large Eddy Simulation (LES)) using both confined and unconfined channels.

To clarify the impact of roughness on the aerodynamic drag coefficient at various flow velocities and particle volume concentrations, it is necessary to set up a task involving the flow around fixed clusters of plate-like particles in both smooth and ribbed configurations to simulate roughness. Additionally, the issue of enhancing particle cohesion by adding adhesive forces should be considered.

The next step for modeling hydrodynamic conditions, imitating the conversion of sawdust to syngas, should involve the simulation of a polyfractional mixture of sawdust with the feature of particle density and equivalent diameter reduction during the calculation process. Special attention should be paid to smaller particles (Geldart A and B), which were out of scope of this study.

Acknowledgement

The research funding from the Ministry of Science and Higher Education of the Russian Federation (Ural Federal University Program of Development within the Priority-2030 Program) is gratefully acknowledged. The licenses for Ansys Fluent®2021 R1 and Rocky DEM 2021 R1 software were provided by PLM Ural LLC.

References

[1] Nascimento F. R. M., Gonzalez A. M., Lora E. E. S., Ratner A., Palacio J. C. E., Reinaldo R., *Bench-scale bubbling fluidized bed systems around the world - Bed agglomeration and collapse: A comprehensive review*, Int J Hydrogen Energy, Vol. 46, No. 36, (2021), P. 18740-18766. doi:10.1016/j.ijhydene.2021.02.086.

[2] Goktepe B., Umeki K., Gebart R., *Does distance among biomass particles affect soot formation in an entrained flow gasification process?*, Fuel Process. Technol., Vol. 141, Pt. 1, (2016), P. 99-105. doi:10.1016/j.fuproc.2015.08.036.

[3] Kashyap M., Gidaspow D., *Circulation of Geldart D type particles: Part IIB—Low solids fluxes: Measurements and computation under dilute conditions*, Chemical Engineering Science, Vol. 66, No. 8, (2011), P. 1649-1670. doi:10.1016/j.ces.2010.12.043.

[4] Geldart D., *Types of gas fluidization*, Powder Technology, Vol. 7, No. 5, (1973), P. 285-292. doi:10.1016/0032-5910(73)80037-3.

[5] Reyes A., Soria J., Saffe A., Zambon M., Echegaray M., Suarez S., Rodriguez R., Mazza G., *Fluidization of biomass: a correlation to assess the minimum fluidization velocity considering the influence of the sphericity factor*, Part. Sci. Technol., Vol. 39, (2021), P. 1-21. doi:10.1080/02726351.2021.1879981.

[6] Bagheri G., Bonadonna C., *On the drag of freely falling non-spherical particles*, Powder Technol., Vol. 301, (2016), P. 526-544. doi:10.1016/j.powtec.2016.06.015.

[7] Ali F., Hamzah K., Khashi'ie N., Waini I., Mustafa N., Long N., *Mechanical and physical properties of sawdust-reinforced epoxy resin composites*, Journal of Southwest Jiaotong University, Vol. 57, (2022), P. 292-299. doi:10.35741/issn.0258-2724.57.3.23.

[8] Chen M., Liu M., Tang Y., *Comparison of Euler-Euler and Euler-Lagrange approaches for simulating gas-solid flows in a multiple-spouted bed*, International Journal of Chemical Reactor Engineering, Vol. 17, (2019). doi:10.1515/ijcre-2018-0254.

[9] *CFD Coupling Technical Manual, ESSS Rocky DEM, Release 2022 R1.1*, S.R.L., (2022).

[10] Ding J., Gidaspow D., *A bubbling fluidization model using kinetic theory of granular flow*, AIChE Journal, Vol. 36, No. 4, (1990), P. 523-538.

[11] Li Y., Che D., Liu Y., *CFD simulation of hydrodynamic characteristics in a multiple-spouted bed*, Chemical Engineering Science, Vol. 80, (2012), P. 365-379. doi:10.1016/j.ces.2012.06.003.

[12] von Berg L., Anca-Couce A., Hochenauer C., Scharler R., *Multi-scale modelling of a fluidized bed biomass gasifier of industrial size (1 MW) using a detailed particle model coupled to CFD: Proof of feasibility and advantages over simplified approaches*, Energy Conversion and Management, Vol. 286, (2023), 117070. doi:10.1016/j.enconman.2023.117070.

[13] Zhang R., Ku X., Yang S., *Study of air-steam gasification of spherocylindrical biomass particles in a fluidized bed by using CFD-DEM coupling with the multi-sphere model*, Energy Conversion and Management, Vol. 276, (2023), 116561. doi:10.1016/j.enconman.2022.116561.

[14] Almohammed N., Alobaid F., Breuer M., Epple B., *A comparative study on the influence of the gas flow rate on the hydrodynamics of a gasB–solid spouted fluidized bed using EulerB–Euler and EulerB–Lagrange/DEM models*, Powder Technology, Vol. 264, (2014), P. 343-364. doi:10.1016/j.powtec.2014.05.024.

[15] Boset L., Wako A., Zewdie B., *Determination of terminal velocity of some agricultural grain using Ansys Rocky DEM-CFD coupling simulation*, Science Development, Vol. 4, No. 2, (2023), P. 28-35. doi:10.11648/j.scidev.20230402.12.

[16] Ganser G.H., *A rational approach to drag prediction of spherical and nonspherical particles*, Powder Technology, Vol. 77, No. 2, (1993), P. 143-152. doi:10.1016/0032-5910(93)80051-B.

[17] Holzer A., Sommerfeld M., *New simple correlation formula for the drag coefficient of non-spherical particles*, Powder Technology, Vol. 184, No. 3, (2008), P. 361-365. doi:10.1016/j.powtec.2007.08.021.

[18] Cao Z., Tafti D.K., Shahnam M., *Development of drag correlation for suspensions of ellipsoidal particles*, Powder Technology, Vol. 369, (2020), P. 298-310. doi:10.1016/j.powtec.2020.05.049.

[19] Liu Z., Ma H., Zhao Y., *CFD-DEM simulation of fluidization of polyhedral particles in a fluidized bed*, Energies, Vol. 14, (2021), 4939. doi:10.3390/en14164939.

[20] Wang T., Gao Q., Deng A., Tang T., He Y., *Numerical and experimental investigations of instability in a spouted bed with non-spherical particles*, Powder Technology, Vol. 379, (2021), P. 231-240. doi:10.1016/j.powtec.2020.10.032.

[21] Di Felice R., *The voidage function for fluid-particle interaction systems*, International Journal of Multiphase Flow, Vol. 20, No. 1, (1994), P. 153-159. doi:10.1016/0301-9322(94)90011-6.

[22] Zastawny M., Mallouppas G., Zhao F., van Wachem B., *Derivation of drag and lift force and torque coefficients for non-spherical particles in flows*, International Journal of Multiphase Flow, Vol. 39, (2012), P. 227-239. doi:10.1016/j.ijmultiphaseflow.2011.09.004.

[23] Sanjeevi Sathish K.P., Kuipers J.A.M., Padding J. T., *Drag, lift and torque correlations for non-spherical particles from Stokes limit to high Reynolds numbers*, International Journal of Multiphase Flow, Vol. 106, (2018), P. 325-337.

[24] Uspensky V. A., *Pnevmaticheskij transport*, 2nd ed., revised and enlarged. Sverdlovsk: Metallurgizdat, Sverdlovsk Branch, (1959), 231 p.

[25] Tang P., Chan H.-K., Raper J.A., *Prediction of aerodynamic diameter of particles with rough surfaces*, Powder Technology, Vol. 147, No. 1B–3, (2004), P. 64-78. doi:10.1016/j.powtec.2004.09.036.

[26] Papkov V., Shadymov N., Pashchenko D., *Gas flow through a packed bed with low tube-to-particle diameter ratio: Effect of pellet roughness*, Physics of Fluids, Vol. 36, (2024), 027127. doi:10.1063/5.0183475.

[27] Bove D., Moliner C., Curti M., Baratieri M., Bosio B., Rovero G., Arato E., *Preliminary tests for the thermo?chemical conversion of biomass in a spouted bed pilot plant*, The Canadian Journal of Chemical Engineering, Vol. 97, (2017). doi:10.1002/cjce.23223.

[28] Stasiak M., Molenda M., Banda M., Gondek E., *Mechanical properties of sawdust and woodchips*, Fuel, Vol. 159, (2015), P. 900-908. doi:10.1016/j.fuel.2015.07.044.

[29] Zhang R., Ku X., Lin J., *Fluidization of the spherocylindrical particles: Comparison of multi-sphere and bond-sphere models*, Chemical Engineering Science, Vol. 253, (2022), 117540. doi:10.1016/j.ces.2022.117540.

M.I. Ershov,
Ural Federal University,
19 Mira st., 620002 Yekaterinburg, Russia
PLM Ural LLC,
16b Metallurgov St., 620131 Yekaterinburg, Russia
Email: ershov1807ershov@yandex.ru,

N.A. Abaimov,
Ural Federal University,
19 Mira st., 620002 Yekaterinburg, Russia
Email: n.a.abaimov@urfu.ru,

A.D. Nikitin,
Ural Federal University,
19 Mira st., 620002 Yekaterinburg, Russia
Email: nikitin.alexander@urfu.ru,

V.G. Tuponogov,
Ural Federal University,
19 Mira st., 620002 Yekaterinburg, Russia
Email: v.g.tuponogov@urfu.ru,

A.F. Ryzhkov,
Ural Federal University,
19 Mira st., 620002 Yekaterinburg, Russia
Email: a.f.ryzhkov@urfu.ru.

Received 01.09.2024, Accepted 15.01.2025, Available online 31.03.2025.